Title Page

Title

Quantifying retinal area in ultra-widefield imaging using a 3-dimensional (3-D) printed eye model

Authors

Luke Nicholson[1,2]

Clara Vazquez-Alfageme[1]

Monica Clemo[1]

Yvonne Luo[1]

Philip G Hykin[1]

James W Bainbridge[1]

Sobha Sivaprasad[1]

Institutional Affiliations

1 National Institute for Health Research Moorfields Biomedical Research Centre, Moorfields Eye Hospital and University College London Institute of Ophthalmology, London, United Kingdom

2 Western Sussex National Health Service Foundation Trust, Worthing, United Kingdom

Financial support: None

Conflict of interest: No conflicting relationship exists for any author

Running head: Quantifying area in ultra-widefield imaging

Corresponding author and reprint requests:

Professor Sobha Sivaprasad

National Institute for Health Research Moorfields Biomedical Research Centre and University College London Institute of Ophthalmology, Moorfields Eye Hospital, 162 City Road, EC1V 2PD, London, United Kingdom

Tel: +4402032994548; Fax: +4402032993738
E-mail: senswathi@aol.com

Abstract

Purpose:

We aim to study the effects of different axial lengths on ultra-widefield imaging to determine the presence of distortion in images despite software correction and calculate an enlargement factor based on angular location.

Design:

Experimental image analysis study.

Study objects:

Three 3-dimensional printed model eyes simulating eyes with axial lengths of 22mm, 24mm and 26mm. Each model has a grid of rings 9 degrees apart centered at the posterior pole

Methods:

Single centre study performed at the National Institute for Health Research Moorfields Biomedical Research Centre, London, United Kingdom. Each model was imaged using Optos 200TX (Optos, Dunfermline, United Kingdom). Two images for each model eye that were corrected using V2 Vantage Pro software (Optos, United Kingdom) were used for analysis and the average values obtained. Each image inter-ring area was measured using ImageJ to obtain a measured image area in pixel and mm^2. This was compared with the true calculated object inter-ring area and an enlargement factor was determined.

Main outcome measures: Measured image inter-ring area in pixels and mm^2. True calculated object inter-ring area in mm^2.

Results:

The enlargement factor of the rings gradually increases towards the periphery with factors of 1.4 at 45 degrees and 1.9 at the equator. The axial lengths did not affect the enlargement factor of the rings imaged in three different model eyes, p=0.9512. The anterior equator exhibits a significant distortion despite the software correction.

Conclusion:

The enlargement factor is dependent on angular location and not axial length. The enlargement factors can be used in clinical practice to more accurately measure area in ultra-widefield imaging.

Text

Introduction

The evolution of ultra-widefield imaging over the past decade has redefined the evaluation and management of retinal diseases. The implications of visualising a wider view of the retina on our understanding of disease mechanisms is significant.[1] We have acquired new knowledge on the impact of peripherally located lesions on the severity of diabetic retinopathy as well as the increasing importance of ultra-widefield imaging in assessing diabetic retinopathy.[2,3] Wide-angled retinal imaging has also enabled us to ascertain the extent of peripheral retinal ischemia in retinal vein occlusions and it was also instrumental in identifying peripheral changes in uveitis and age related macular degeneration.[4–6]

It is believed that using an elliptical mirror with a focal point at the plane of the iris, the Optos ultra-widefield system (Optos 200TX; Optos, Dunfermline, United Kingdom) can potentially view 200 degrees of the retina in a single capture, at least three times more than the view obtained with montaged 7-field standard fundus images.[7]

Despite marked progress in the field, care needs to be taken to assess the quality and reliability of the images obtained. So far, three unique observations have been made. Firstly, obtaining a wide view of the three–dimensional retina and displaying the image obtained in a flat two dimensional image causes a projection distortion of the ultra-widefield image produced.[4] Secondly, a horizontal stretch over the entire image that magnifies into the periphery has also been reported in uncorrected images.[8,9] Finally, the impact of different axial lengths on the images produced can vary the imaged size by almost 10%.[10]

The ultra-widefield system is unique and still evolving, and it is important to rectify these flaws to realise the full potential of this system. Significant efforts have been made to measure and quantify area in ultra-widefield images. Precise quantification of area is challenging and the concept of a pixel ratio was used for the ischemic index while comparisons to disc area used in the concentric rings method.[11,12] Spaide et al suggested an azimuthal projection technique and the Optos software now incorporates its own stereographic projection software to correct the peripheral distortion and the horizontal stretch.[4,13] The stereographic projection software has been studied and although the ischemic index in the corrected images are comparable with uncorrected images, the variation can be as high as 14.8%.[14]

Acknowledging that the Optos system can view up to 200 degrees in a single image, 20 degrees of the anterior equatorial retina will also be included in the image. It is perfectly reasonable to assume that a hemisphere will have predictable projection errors. However, if we place a set of annular rings in a sphere, the equator will have the largest area and the area of the annulus anterior and posterior to the equator will be smaller. This can be explained using the spherical cap formula on a sphere with a radius of 11mm. The area for three annulus subtending 10° such as 40-50°, 80-90° and 130-140°, which represents an annulus straddling 45°, 90° and 135° can be calculated. The area for these are $93.7mm^2$, $132.5mm^2$ and $93.7mm^2$. The area increases from the posterior pole towards the equator and subsequently decreases towards to anterior pole. This is particularly important when measuring area beyond the equator as the size decreases although projection artefacts are likely to increasingly distort the images.

The primary aim of this study was to utilise a 3-D printed eye model to study if there remains a distortion in the image produced and if so, suggest ways to rectify them to enable quantification of lesion dimensions accurately. We also intend to study the effects of axial length on the image produced and the concept of an anterior equator distortion by studying the enlargement factor based on the angular location in the image.

Methods

This image analysis study was performed in the National Institute for Health Research Moorfields Biomedical Research Centre and University College London Institute of Ophthalmology, London, United Kingdom.

Model eye

Three model eyes of different axial lengths were developed and 3D printed by 3DPrintUK, London using an EOS P100 (EOS Ltd, Germany) with material from Nylon PA2200. The models were spheres with an 8mm aperture simulating the pupil. The thickness of the model eye wall is 2mm. A sulcus was created to accommodate a three piece +21.0 Dioptre intraocular lens. Therefore, the position of the lens would simulate a lens positioned at the sulcus. The lens used was the Acrysof multi-piece MA60AC (Alcon, Texas, USA) with a 6.0mm optic and a reported spherical aberration of +0.14 +/- 0.09µm.[15] A grid composed of multiple concentric rings centred at the posterior pole were made for each model eye. The grooves are 0.4mm in width. Each ring is 9 degrees apart, beginning in the posterior pole and extending to the ‘pupil’ or aperture. These model eyes consist of three different internal diameters and thus simulating three different axial lengths, 22mm, 24mm and 26mm. Figure 1 is an example of the design for a model eye with an axial length of 24mm. The true object area of each ring which is the inter-ring area including the grooves can be calculated using the known dimensions by applying the spherical cap formula. As the rings are positioned 9 degrees apart, the area of ring 5 for example, which is located between 36 and 45 degrees from the posterior pole, has a larger true object area in the 26mm model eye than the 22mm model eye

Image Acquisition

Each model eye was imaged using the Optos 200TX (Optos, Dunfermline, United Kingdom). The model eyes were positioned at the imaging area and the ‘green in-focus’ light was obtained prior to obtaining a central image. Each image output is automatically corrected for three-dimension to two-dimension projection errors by the V2 Vantage Pro software (Optos, Dunfermline, United Kingdom) which utilises stereographic projection techniques.

Image Analysis

Two central images of each model eye resulting in a total of six images were used for analysis. The grid was traced using Photoshop CS2 (Adobe, San Jose, USA). The measurements were made at the outer boundary of each groove as this is better delineated. The pixel area of each ring area were measured using the magic wand tool in Image J.[13] This is exhibited in Figure 2. The true calculated area for the central circle is divided by the measured pixel area to obtain the equivalent area for each pixel. The central circle at the posterior pole was used as a reference as the distortion at zero degrees is minimal.[8,16] The measured image area was then determined by multiplying the measured pixel area with the equivalent area for each pixel. The images obtained were divided into four quadrants, superior, right, inferior and left. The superior and inferior quadrants represent the vertical component and the right and left quadrants represent the horizontal component. The average measurements of the quadrants were obtained from two images of each model eye using ImageJ.

Image Enlargement Factor

The average measured image area of each ring from the two images for each axial length were divided by the true calculated area to obtain an enlargement factor. This was performed for each respective model eye. The enlargement factor obtained for each ring in each model eye was used to assess if distortion is still present in corrected ultra-widefield images. The enlargement factor was also calculated using the same method for the vertical and horizontal component of each inter-ring area for the three different model eyes.

Influence of axial lengths

The measured image pixel area of each ring for each model eye were plotted against the degrees from the posterior pole. This was repeated with the true calculated area for each ring for each model eye of different axial lengths. This was done to understand the effects axial length and angular location has on peripheral distortion.

Anterior equator distortion

To determine if the anterior equator distortion is present, the measured image pixel area of ring 10 (pre-equator) in all six images used from three different axial lengths were compared with the area of ring 11 (anterior equator) in each respective image. The inter-ring area for each annulus between 81-90° and 90-99° which are represented by rings 10 and 11 are calculated to be 118.9mm^2.

Statistical analysis

Kruskal-Wallis test was used to assess statistical significance between the enlargement factors between the three different axial lengths. Linear regression was used to assess the relationship between the enlargement factor of each inter-ring area and the location of the rings. Mann-Whitney U test was used to assess the differences in pre-equatorial and post equatorial rings. A significance level was set at 0.05.

Results

1. Image enlargement factor

The inter-ring area enlargement factors for each model eye of simulated axial lengths of 22mm, 24mm and 26mm are detailed in table 1. A graphical representation of this is provided in figure 3. There is still a graduated increase in distortion which is related to the angular position from the posterior pole, R^2=0.9739, p=<0.0001. There were no significant difference between the enlargement factors for different axial lengths, p=0.9512. By using the 24mm model, the percentage of the area of each ring over the entire image was identified and the enlargement factor weighted to the percentage covered by each ring was determined to obtain a global enlargement factor. This was found to be 1.62, and thus a conversion factor (1/enlargement factor) of 0.62. The mean enlargement factor for the vertical component was 1.54 while that of the horizontal component was 1.37, p=0.0629.

2. Influence of axial length

The enlargement ratio followed a similar pattern with no statistically significant difference between the three different axial lengths, p=0.9512. The exact measurements are tabulated in Table 1 and this is further presented in Figure 3. Figure 4 details the measured image area in pixels and the true calculated object inter-ring area for each ring in each of the three models.

3. Anterior equator distortion

The mean area of ring 10 (pre-equator) was 14915 pixels 95% CI [12916, 16915]. The mean area of ring 11 (anterior equator) was 15827 pixels 95% CI [13454, 18201]. The difference between the two was statistically significant, p=0.0025.

Discussion

Numerous methods have been utilised to study image distortion in ultra-widefield imaging but this is the first reported study whereby 3-D printed model eyes have been used with the analysis of the influence of varying axial lengths on the image produced.[8–10] Previous reports have used known sizes such as the Argus implant or the optic disc but using a 3-D printed model eye, more detailed analyses can be performed.[9,10,16] From our study, we have identified several key findings. Firstly, despite software correction, there is still an increasing distortion towards the periphery. The average enlargement factor at 9-18 degrees from posterior pole is 1.13 and 1.90 at 81-90 degrees from the posterior pole. We have also identified that the enlargement factors for the three different axial lengths follows a similar curve as seen in figure 3. Therefore, these enlargement factors may be used in all eyes independent of their axial lengths. This finding is due to the fact that angles were used to delineate the rings in the model eye, i.e. each ring is 9 degrees from the next. Therefore, the enlargement factor is dependent on the angular location. Although, the size is different between model eyes, the angular position of each segment is similar between different axial lengths and so the enlargement ratio is similar. Secondly, although the true calculated object area for each ring in the three different models are different, the measured image pixel size of each ring for the three different axial lengths are almost identical as depicted in figure 4. This helps explain the finding by Sagong et al that reported the size of objects can vary as much as 10% depending on axial lengths.[10] The larger the axial length, there is more 'shrinkage' of a similar sized object and vice versa. We propose that this is related to the mechanism by which the ultra-widefield system obtains images and therefore theoretically the inside of a football and a ping pong ball will look rather similar in the image produced despite obvious differences in size.

We have also shown that the distortion is still present and larger towards the periphery which has an implication towards the ischemic index measurements utilised in previous studies. As the ischemic index takes the percentage of non-perfused retina as a whole, variability in the distribution of retinal non-perfusion will affect the corrected ischemic index as described by Tan et al, whereby the difference ranged from -5.9% to 14.8%.[14] This is due to the variability in the enlargement factor which is based on the angle from the posterior pole.

This study also confirms the presence of an anterior equator enlargement and that it contributes to the distortion obtained. This anterior equator phenomenon is an interesting concept especially when imaging technology improves and allows more peripheral imaging. Our study suggests that the anterior equator appears to follow the same projection curve irrespective of axial lengths with no reduction in size. We acknowledge that the numbers are small, six sets of measurements from three different models.

Interestingly, in the uncorrected images, a horizontal stretch was identified using different models.[8,9] The new software (V2 Vantage Pro, Optos) corrects for this distortion. Although, there appears to be a trend for the vertical component of images to be stretched more than the horizontal in the corrected images but this was not found to be significant in our study.

There are several limitations in our study and this includes the assumption that in practice, the eye is a perfect sphere like the model eyes used. In reality, variations in ocular shape and deviation from a perfect sphere will affect the accuracy in translating our findings into practice. Secondly, only three different axial lengths were studied.

For clinical use, using our data, we have produced an enlargement factor based on the position in the image. This can be helpful in clinical practice to obtain an approximate size of lesions in varying positions of an ultra-widefield image. We acknowledge that for a more precise quantification of area, Croft et al have proposed and proven that projecting the image into a three-dimensional model and using spherical trigonometry, accurate measurements can be made.[16] We acknowledge that using this method, it may be more accurate however from a practical point in clinical practice, it will be difficult.

We appreciate that in digital imaging, the sizes in ultra-widefield imaging are in pixels and therefore any object in the posterior pole whereby the distortion is less can be used as a reference.[8,16] For example, in an image with an optic disc area of 2.54mm^2 that measures 800 pixels, a lesion at 85-90 degrees from the centre measuring 6000 pixels, the actual size of the lesion should be approximately 10.10mm^2 instead of 19.05mm^2, using a conversion factor of 0.53.

The concentric rings method has been reported as a reliable method in determining retinal non-perfusion.[12] By superimposing the rings, an ultra-widefield image of the retina and the image of a 24mm model eye, we have summarised the enlargement factor and angle imaged for each of the concentric rings. This is further detailed in Table 2.

This revelation of a significant magnification in the periphery has also been suggested by Oishi et al[8] however by identifying a specific enlargement factor and thus a conversion factor for images, we are now able to better quantify area in ultra-widefield imaging. In previous studies, the maximum area identified in ultra-widefield imaging were 1148mm^2 and 1856mm^2 by using a standard disc area of 2.54mm^2.[12,17] This is a unlikely to be accurate and mirrors a peripheral distortion as the predicted size of the retina including the optic disc has been mathematically determined to be 1133.8mm^2 and the area of perfused area in normal retina in ultra-widefield angiography was found to be 977.0mm^2.[18,19] By using the global conversion factor of 0.62, these values from previous studies would be converted to 711.8mm^2 and 1150.7mm^2 which is more realistic. Furthermore, previous

In conclusion, ultra-widefield imaging is used frequently in clinical research to assess the peripheral retina and an accurate quantification of area is required to further validate the results obtained. The enlargement factor is based on angular location despite varying axial lengths. We propose a conversion factor that can be used to improve the accuracy in quantifying area in ultra-widefield images after incorporating corrections for peripheral and anterior equator distortion.

References

1. Nagiel A, Lalane RA, Sadda SR, Schwartz SD. ULTRA-WIDEFIELD FUNDUS IMAGING: A Review of Clinical Applications and Future Trends. *Retina*. 2016;36(4):660-678.

2. Silva PS, Dela Cruz AJ, Ledesma MG, et al. Diabetic Retinopathy Severity and Peripheral Lesions Are Associated with Nonperfusion on Ultrawide Field Angiography. *Ophthalmology*. 2015;122(12):2465-2472. d

3. Ghasemi Falavarjani K, Wang K, Khadamy J, Sadda SR. Ultra-wide-field imaging in diabetic retinopathy; an overview. *J Curr Ophthalmol*. 2016;28(2):57-60.

4. Spaide RF. Peripheral areas of nonperfusion in treated central retinal vein occlusion as imaged by wide-field fluorescein angiography. *Retina*. 2011;31(5):829-837.

5. Karampelas M, Sim DA, Chu C, et al. Quantitative analysis of peripheral vasculitis, ischemia, and vascular leakage in uveitis using ultra-widefield fluorescein angiography. *Am J Ophthalmol*. 2015;159(6):1161-1168.e1.

6. Lengyel I, Csutak A, Florea D, et al. A Population-Based Ultra-Widefield Digital Image Grading Study for Age-Related Macular Degeneration-Like Lesions at the Peripheral Retina. *Ophthalmology*. April 2015.

7. Kaines A, Oliver S, Reddy S, Schwartz SD. Ultrawide angle angiography for the detection and management of diabetic retinopathy. *Int Ophthalmol Clin*. 2009;49(2):53-59.

8. Oishi A, Hidaka J, Yoshimura N. Quantification of the image obtained with a wide-field scanning ophthalmoscope. *Invest Ophthalmol Vis Sci*. 2014;55(4):2424-2431.

9. Nicholson L, Goh LY, Marshall E, et al. Posterior Segment Distortion in Ultra-Widefield Imaging Compared to Conventional Modalities. *Ophthalmic Surg Lasers Imaging Retina*. 2016;47(7):644-651.

10. Sagong M, van Hemert J, Olmos de Koo LC, Barnett C, Sadda SR. Assessment of accuracy and precision of quantification of ultra-widefield images. *Ophthalmology*. 2015;122(4):864-866.

11. Tsui I, Kaines A, Havunjian MA, et al. Ischemic index and neovascularization in central retinal vein occlusion. *Retina*. 2011;31(1):105-110.

12. Nicholson L, Vazquez-Alfageme C, Ramu J, et al. Validation of Concentric Rings Method as a Topographic Measure of Retinal Nonperfusion in Ultra-Widefield Fluorescein Angiography. *Am J Ophthalmol*. 2015;160(6):1217-1225.e2.

13. Schneider CA, Rasband WS, Eliceiri KW. NIH Image to ImageJ: 25 years of image analysis. *Nat Methods*. 2012;9(7):671-675.

14. Tan CS, Chew MC, van Hemert J, Singer MA, Bell D, Sadda SR. Measuring the precise area of peripheral retinal non-perfusion using ultra-widefield imaging and its correlation with the ischaemic index. *Br J Ophthalmol*. July 2015.

15. Moorfields IOL Study Group, Allan B. Binocular implantation of the Tecnis Z9000 or AcrySof MA60AC intraocular lens in routine cataract surgery: prospective randomized controlled trial comparing VF-14 scores. *J Cataract Refract Surg*. 2007;33(9):1559-1564.

16. Croft DE, van Hemert J, Wykoff CC, et al. Precise montaging and metric quantification of retinal surface area from ultra-widefield fundus photography and fluorescein angiography. *Ophthalmic Surg Lasers Imaging Retina*. 2014;45(4):312-317.

17. Wykoff CC, Brown DM, Croft DE, Major JC, Wong TP. Progressive retinal nonperfusion in ischemic central retinal vein occlusion. *Retina*. 2015;35(1):43-47.

18. Taylor E, Jennings A. Calculation of total retinal area. *Br J Ophthalmol*. 1971;55(4):262-265.

19. Singer M, Sagong M, van Hemert J, Kuehlewein L, Bell D, Sadda SR. Ultra-widefield Imaging of the Peripheral Retinal Vasculature in Normal Subjects. *Ophthalmology*. 2016;123(5):1053-1059.

Figure Captions

Figure 1: The design of the model eye with an axial length of 24mm with section A-A representing the coronal plane and section B-B, the sagittal plane (Top left). The radius of the model is 13mm, R13 (top right). The walls of the model eye have a thickness of 2mm. Each model is made up of multiple rings centered at the posterior pole with each ring separated by nine degrees as in the image. Top right image represents the sagittal plane and bottom left image represents the coronal plane. Bottom right image represents the model eye viewed externally.

Figure 2: The grids in the original image (left) is traced using Photoshop CS2 (Adobe, San Jose, USA) (middle). In this example, the line thickness is set at 5 pixels for ease of the reader however, in determining the area, this was set at 1 pixel for increased accuracy. The traced image which was used to determine the area of each ring in pixels using ImageJ (right).

Figure 3: Graph representing the enlargement factors of model eyes with simulated axial lengths of 22mm, 24mm and 26mm. The results were plotted against an x-axis of the angles (in degrees) from the posterior pole of the model eye.

Figure 4: The measured pixel area of each ring (Left) and the true calculated area in mm^2 of each ring (Right) for the model eyes with axial lengths of 22mm, 24mm and 26mm.

Acknowledgements / Disclosures

a (Funding Support) :

No funding was received for the work submitted. The authors have not received funding for the work submitted. Prof Bainbridge is a National Institute for Health Research (NIHR) Research Professor.

b (Financial Disclosures) :

Dr Nicholson, Dr Vazquez-Alfageme, Ms Clemo, and Dr Luo has nothing to disclose.

Dr Hykin has received Grants from Novartis (Surrey, United Kingdom), Allergan (Irvine, California) and Bayer (Leverkusen, Germany); is on the advisory board and receives speaker fees from Novartis and Bayer.

Prof Bainbridge has received research grants from Novartis (Surrey, United Kingdom) and Bayer (Leverkusen, Germany), and receive consultancy fees from Astellas and MeiraGTx Ltd.

Prof Sivaprasad has received Grants from Novartis (Surrey, United Kingdom), Allergan (Irvine, California) and Bayer (Leverkusen, Germany); is on the advisory board and receives speaker fees from Novartis, Allergan and Bayer.

Table 1: The enlargement factors for each model eye of axial lengths 22mm, 24mm, and 26mm

Angle (degrees)	Ring number	Axial length of 22mm	Axial length of 24mm	Axial length of 26mm
0-9	1	1.00	1.00	1.00
9-18	2	1.15	1.10	1.12
18-27	3	1.19	1.15	1.15
27-36	4	1.25	1.23	1.23
36-45	5	1.33	1.30	1.31
45-54	6	1.40	1.37	1.36
54-63	7	1.51	1.47	1.47
63-72	8	1.62	1.61	1.62
72-81	9	1.74	1.76	1.73
81-90	10	1.90	1.87	1.93
90-99	11	2.06	1.97	2.04

Figure 1

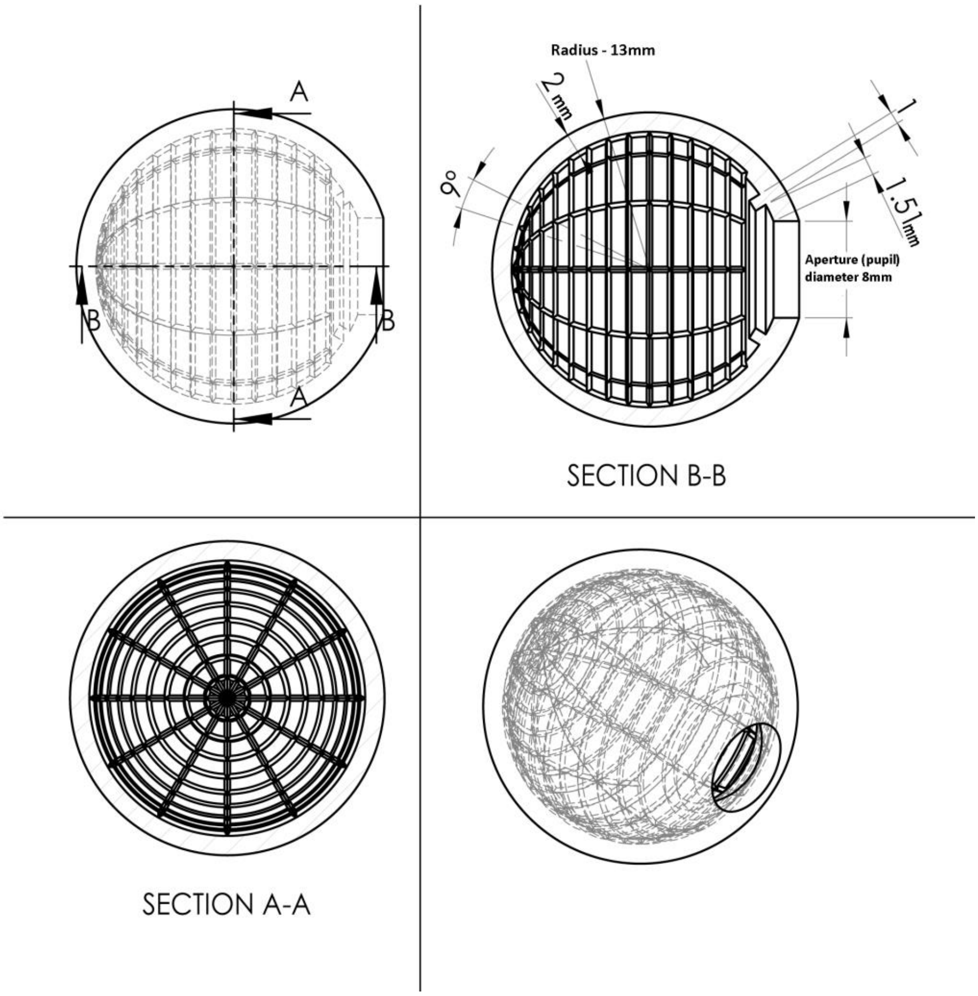

Figure 2

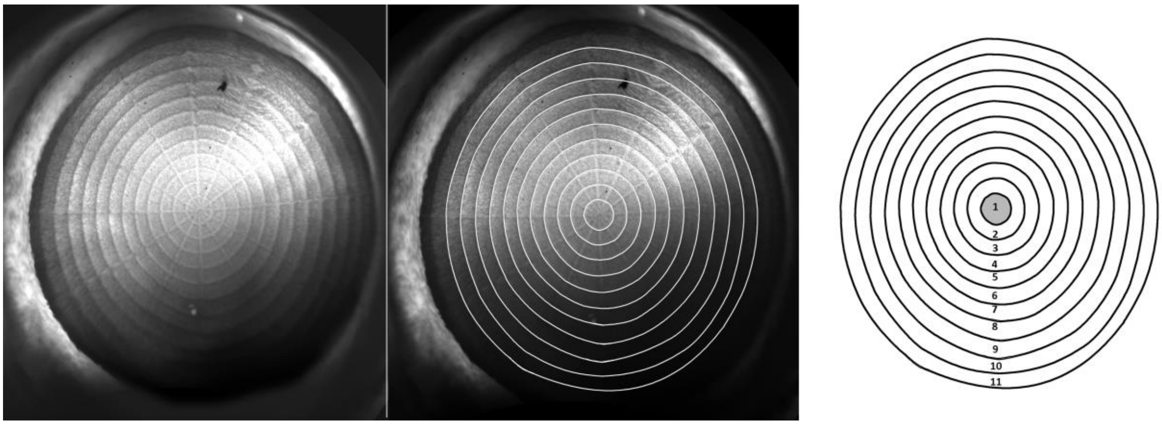

Figure 3

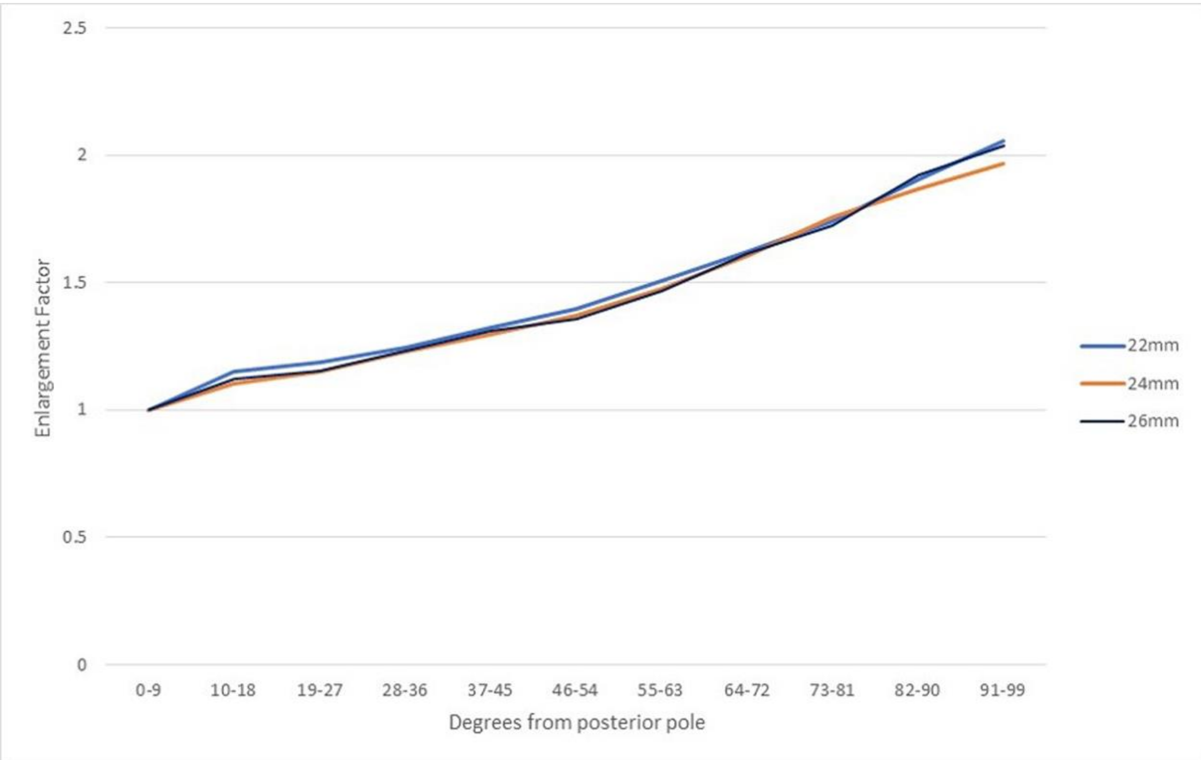

Figure 4

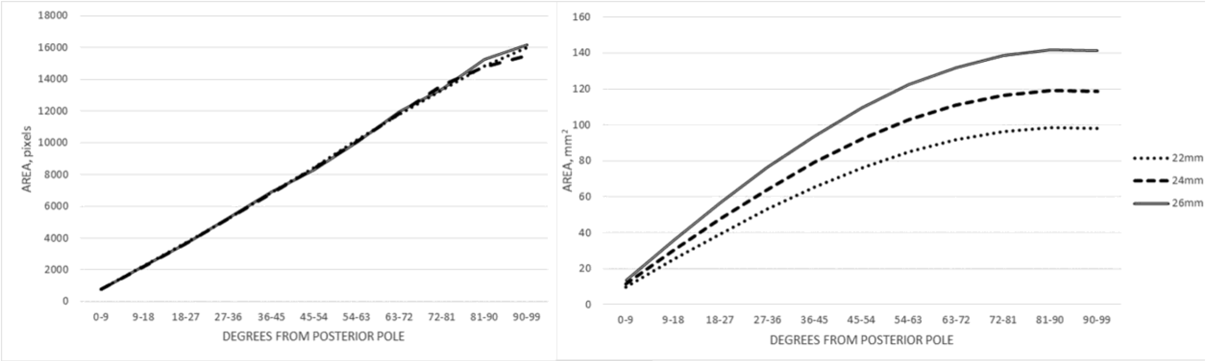

AREA, pixels
0-9 9-18 18-27 27-36 36-45 45-54 54-63 63-72 72-81 81-90 90-99
DEGREES FROM POSTERIOR POLE
AREA, mm2
DEGREES FROM POSTERIOR POLE
22mm
24mm
26mm